OPEN ACCESS
IOP Publishing
Journal of Physics D: Applied Physics
J. Phys. D: Appl. Phys. **56** (2023) 305103 (10pp)
https://doi.org/10.1088/1361-6463/acd06b

Carrier removal rates in 1.1 MeV proton irradiated α-Ga_2O_3 (Sn)

A Y Polyakov[1], V I Nikolaev[1,2], A I Pechnikov[1,2], P B Lagov[1,3], I V Shchemerov[1], A A Vasilev[1], A V Chernykh[1], A I Kochkova[1], L Guzilova[1,2], Yu S Pavlov[3], T V Kulevoy[4], A S Doroshkevich[5], R Sh Isaev[5], A V Panichkin[1] and S J Pearton[6,*]

[1] National University of Science and Technology MISiS, Moscow, Leninsky pr. 4, Moscow 119049, Russia
[2] Perfect Crystals LLC, 38k1 Toreza Avenue, off. 213, Saint Petersburg 194223, Russia
[3] Laboratory of Radiation Technologies, A. N. Frumkin Institute of Physical Chemistry and Electrochemistry Russian Academy of Sciences (IPCE RAS), Moscow 119071, Russia
[4] National Research Centre 'Kurchatov Institute'—KCTEP, 25, Bolshaya Cheremushkinskaya Str, Moscow 117218, Russia
[5] Joint Institute for Nuclear Research, Joliot-Curie 6, Dubna, Moscow Region 141980, Russia
[6] Department of Materials Science and Engineering, University of Florida, Gainesville, FL 32611, United States of America

E-mail: spear@mse.ufl.edu

Received 2 February 2023, revised 27 March 2023
Accepted for publication 26 April 2023
Published 9 May 2023

Abstract

Films of α-Ga_2O_3 (Sn) grown by halide vapor phase epitaxy on sapphire with donor densities in the range 5×10^{15}–8.4×10^{19} cm^{-3} were irradiated at 25 °C with 1.1 MeV protons to fluences from 10^{13} to 10^{16} cm^{-2}. For the lowest doped samples, the carrier removal rate was ~35 cm^{-1} at 10^{14} cm^{-2} and ~1.3 cm^{-1} for 10^{15} cm^{-2} proton fluence. The observed removal rate could be accounted for by introduction of deep acceptors with optical ionization energies of 2 eV, 2.8 eV and 3.1 eV. For samples doped at 4×10^{18} cm^{-3}, the initial electron removal rate was 5×10^3 cm^{-1} for 10^{15} cm^{-2} fluence and ~300 cm^{-1} for 10^{16} cm^{-2} fluence. The same deep acceptors were observed in photocapacitance spectra, but their introduction rate was orders of magnitude lower than the carrier removal rate. For the heaviest doped samples, the electron removal rate was close to that for the 4×10^{18} cm^{-3} sample. The radiation tolerance of lightly doped α-Ga_2O_3 is higher than for similarly doped β-Ga_2O_3 layers.

Supplementary material for this article is available online

Keywords: carrier, removal, rates, proton, irradiated, Ga_2O_3

(Some figures may appear in colour only in the online journal)

* Author to whom any correspondence should be addressed.

1. Introduction

The ultra-wide bandgap semiconductor Ga_2O_3 is attracting interest because of the potential for application in high-power electronic devices and in deep UV efficient solar-blind photodetectors [1–6]. The main thrust of the work has concentrated on the thermodynamically stable monoclinic β-Ga_2O_3 polymorph with its high electric breakdown field of $\sim$8 MV cm^{-1}, exceeding by several times those of GaN and SiC. Ga_2O_3 also has the largest bandgap of semiconductors able to be grown in bulk form from melts and the capability for excellent quality films grown on native β-Ga_2O_3 substrates by all standard versions of epitaxy [1, 2].

There is also interest in the metastable corundum α-Ga_2O_3 polymorph [1, 2, 4–6]. This has a higher bandgap of 5.1 eV versus 4.8 eV for β-Ga_2O_3, higher symmetry (corundum versus monoclinic), the existence of corundum structure metal oxides showing p-type conductivity and available for fabrication of useful heterostructure devices, and finally, the possibility to grow on sapphire (α-Al_2O_3) substrates [1, 4, 5, 7–20]. For α-Ga_2O_3, high quality films grown by halide vapor phase epitaxy (HVPE) [8–10, 14, 18–20] or mist chemical vapor deposition [11, 15] have been demonstrated, along with fabrication of power rectifiers with promising characteristics [8, 21]. Power rectifiers based on *p-n* heterojunctions have also been reported [21]. Additional advances have included epitaxial lateral overgrowth [22], growth using strain relief layers of graded composition α-$(Al_xGa_{1-x})_2O_3$ [23] and deposition using α-Cr_2O_3 underlayers [24, 25] to relieve strain which normally causes a high dislocation density.

One of the expected benefits of devices based on wide-bandgap materials is their high radiation tolerance related to the tight bonding. For β-Ga_2O_3, results have been described previously [16, 26–28]. The general conclusion is the radiation tolerance of β-Ga_2O_3 exceeds that of Si or GaAs and is at least comparable to GaN or SiC [16, 26, 27].

For the metastable α-Ga_2O_3, radiation studies have just begun. Rutherford back-scattering experiments performed for implantation of α-Ga_2O_3 and β-Ga_2O_3 with heavy ions suggest their radiation tolerance could be higher than GaN [29]. We published the results of the effects of proton irradiation of undoped semi-insulating films of α-Ga_2O_3 on their electrical properties [30]. These results point to the important influence of Ga vacancy and Ga–O divacancy defects and their segregation near the surface. In this paper we report studies of proton irradiation effects on electrical properties of HVPE grown *n*-type films as a function of Sn donor concentration.

2. Experimental

The samples were grown by HVPE on basal plane (0001) sapphire at 500 °C, with a fixed VI/III mole flow ratio of 4.2 and an average growth rate of 2.8 μm h^{-1}. The thickness was $\sim$5 μm. Sn doping was performed using a volatile salt of Sn. The crystalline structure was characterized by x-ray diffraction (XRD) θ–2θ pattern measurements and magnitude of the full width at half maximum (FWHM) of double-crystal geometry high-resolution XRD rocking curves for symmetric and skew-symmetric reflections of (0006)/(10–18). The FWHM was 13 arcmin for the (0006) reflection and 14 arcmin for the (10–18) reflections. The net donor doping was varied by varying the Sn atom flow into the reactor. Three doping levels were studied: sample S1 with net donor concentration of $\sim 5 \times 10^{15}$ cm^{-3}, sample S2 with net donor concentration of 3.5×10^{18} cm^{-3}, and sample S3 with net donor concentration of 8×10^{19} cm^{-3}. Only the upper $\sim$1–1.5 μm of the films was intentionally doped. The control of the doping level depended on the density of defects and on Sn source depletion during the growth [18, 24, 25].

For characterization, Ohmic Ti/Au contacts (20 nm/80 nm) of $\sim$2 mm-wide stripes going from one end to the other of the film were deposited by e-beam evaporation with a shadow mask and annealed at 300 °C in N_2. Circular semi-transparent Ni Schottky diodes 1 mm in diameter and 20 nm thick were deposited by e-beam evaporation via a shadow mask. The samples before and after irradiation with various fluences of 1.1 MeV protons were characterized by current–voltage (*I–V*) between 100 K and 450 K, capacitance–voltage (*C–V*) and capacitance versus frequency (*C–f*) measurements in the dark and under monochromatic illumination with a set of light emitting diodes (LEDs) with peak photon energies ranging from 1.35 eV to 4.5 eV. Admittance spectra (AS) [31] at frequencies from 20 Hz to 2 MHz in the temperature range 100 K–450 K, and by deep level transient spectroscopy (DLTS) [20, 31]. Details of the experimental setups can be found elsewhere [18, 20, 24, 25, 32–37].

Proton irradiations were carried out at room temperature with energies 1.1 MeV, flux of 10^{11}–10^{12} cm^{-2} s^{-1} and fluences 10^{13}, 10^{14}, 10^{15} or 10^{16} cm^{-2}. The linear accelerator I-2 serving as a proton injector of a cyclotron with proton energy up to 10 GeV was used [32, 35–37]. The proton energy inside the accelerator was 24.6 MeV, the proton beam exited through a port into air, with the energy reduced to 22.5 MeV and further attenuated to the required energy using a set of calibrated metal foils (degraders) reducing the energy to 1.1 MeV. The projected range of protons at this energy is 9.88 μm, ending in the sapphire substrate, with a longitudinal straggle of 0.56 μm. However, the energy loss over most of the epithickness is relatively uniform. The electronic or ionizing energy loss under these conditions is $\sim$130 MeV cm^2 mg^{-1}, and 4.8×10^{-2} MeV cm^2 mg^{-1} for non-ionizing energy loss [38]. The stopping powers are $\sim$3 MeV mm^{-1} for electronic processes and $\sim 10^{-3}$ MeV mm^{-1} for nuclear processes, so the energy loss is dominated by the former. The defect states we detect are mostly created by the non-ionizing energy-loss, which create primary defects by both the initial atomic collisions and by the cascade generation due to nucleus recoil, and secondary defects caused by diffusion of primary point defects. The carrier removal rate, R_C, was obtained from:

$$R_C(i) = (n_s(i) - \frac{n_s(i+1)}{\Phi(i+1) - \Phi(i)} \quad (1)$$

where $\Phi(i)$ is the proton fluence in the *i*th irradiation, $n_s(i)$ is the carrier concentration averaged over the width $w(i)$ of

the space charge region (SCR) corresponding to the fluence $\Phi(i)$, $n_s(i+1)$ is the average concentration in the same part of the SCR $w(i)$ after irradiation with the next fluence $\Phi(i+1)$ and i is the running index of consecutive irradiations. The reason for the more complicated than usual definition of the removal rate is that the concentration profiles deduced from C–V measurements are not exactly flat and in many cases irradiation with a higher dose leaves the part of the SCR where the carriers were present before irradiation partly or fully depleted after irradiation. This is a consequence of defect formation varying with depth and increasing towards the surface.

3. Results and discussion

We start with the lowest doped sample S1. Figure 1 presents room temperature C–f characteristics before and after irradiation with different fluences of protons. Figure 2 displays the evolution with proton dose of the charged centers concentration profiles calculated from $1/C^2$ –V [31] measured at 25 °C at 1 kHz. Figure 3 compares the I–V characteristics before and after irradiation with 10^{15} cm^{-2} fluence. From figure 1, before irradiation the C–f characteristic shows two steps corresponding to two types of donor centers with ionization energy 0.25 eV (fast donors, the 1 kHz step) and 0.35 eV (slow donors, the step in C–f near 200 Hz) [8]. The concentrations of both types of species are similar, but the slow 0.35 eV centers are predominant in the near-surface region whereas the shallow 0.25 eV donors dominate deeper inside the sample (determined by C–V profiling at 300 Hz and 1 kHz and illustrated by figure S1 of supplementary material). The concentration of fast donors probed at 1 kHz was 4.6×10^{15} cm^{-3} and decreased deeper into the sample. Irradiation with fluence of 10^{14} cm^{-2} suppressed the contribution of slow donors (figure 1) and led to depletion of the top ~1 μm of the film (figure 2).

Further irradiation with 10^{15} cm^{-2} protons decreased the concentration of fast 0.25 eV donors to 1.5×10^{14} cm^{-3} (figure 2). All the shallow donors in the top 1.2 μm of the film should have been compensated after irradiation with 10^{14} cm^{-2} fluence, which indicates the average carrier removal rate for that fluence is ~35 cm^{-1} (see equation (1) and table 1).

Similarly, for the dose of 10^{15} cm^{-2}, all donors between 1.2 μm and 1.5 μm have been removed, with an average removal rate of $\geqslant$1.3 cm^{-1}. Thus, the effective electron removal rate for the bulk portion of the film decreased with increasing fluence from ~40 to ~1 cm^{-1}. This was accompanied by a strong increase of the series resistance in forward I–V characteristics from ~200 Ω to 2.5×10^3 Ω after irradiation with 10^{15} cm^{-2} protons. Figures 4(a) and (b) compares the photocapacitance spectra measured before irradiation and after irradiation with 10^{15} cm^{-2} protons. The y-axis represents the $\Delta C_{ph}/C_{dark}$ multiplied by $2N_d$, where ΔC_{ph} is the difference between the photocapacitance induced by illumination

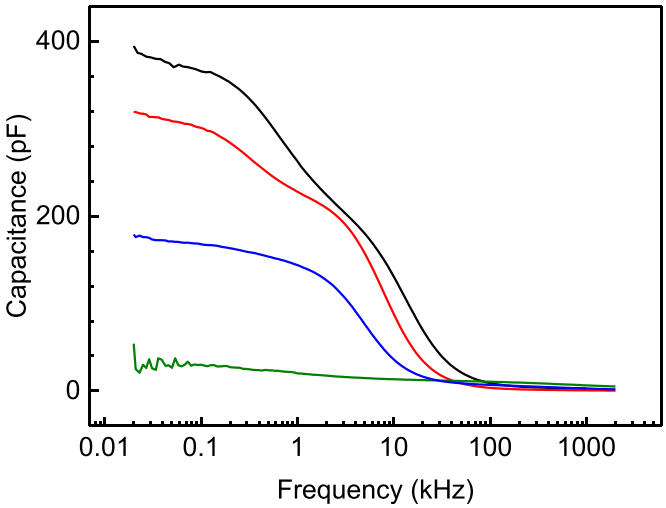

Figure 1. Room temperature C–f characteristics of the lightly doped C1 sample before irradiation (black line), after irradiation with 10^{13} cm^{-2} (red line), 10^{14} cm^{-2} (blue line), and 10^{15} cm^{-2} (olive line) of 1.1 MeV protons.

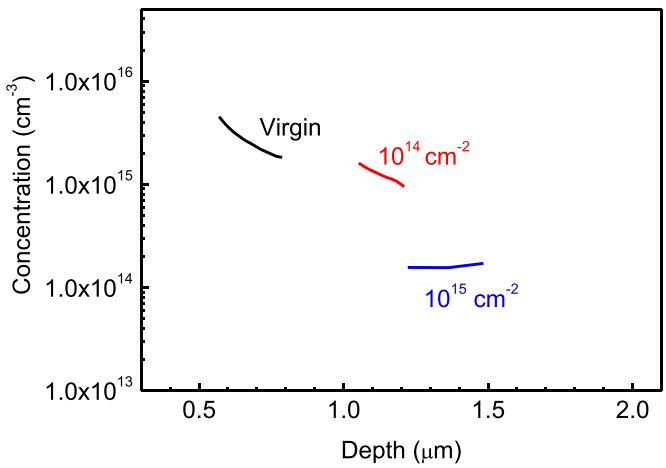

Figure 2. Concentration profiles calculated for lightly doped sample S1 from C–V profiling at room temperature and 1 kHz before irradiation (black line), after irradiation with 10^{14} cm^{-2} (red line), and 10^{15} cm^{-2} (blue line).

from LEDs with the chosen peak photon energy (i.e. capacitance under illumination minus dark capacitance), C_{dark} is the dark capacitance, N_d is the net 'bulk' donor concentration derived from C–V profiling at 1 kHz [18]. This way the photocapacitance signal can be approximately converted to the density of centers contributing to photocapacitance [18, 38].

There are three major deep acceptors with optical thresholds near 2 eV, 2.8 eV and 3.1 eV. The centers with optical threshold of 2.8 eV were persistent at room temperature and had a barrier for capture of electrons, as shown by blue open triangles obtained after switching the light off and applying the forward bias of +2 V for 10 s [18]: the photoconcentration for these photons did not decrease after switching

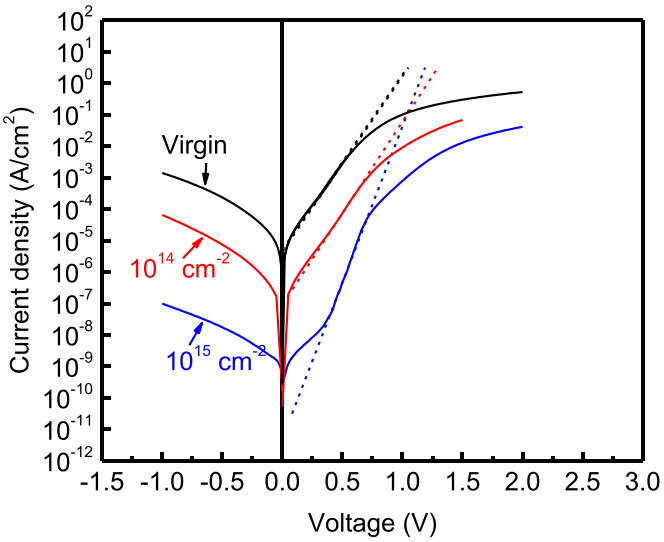

Figure 3. Room temperature *I–V* characteristics of lightly doped sample S1 before irradiation (black line), after irradiation with 10^{14} cm^{-2} (red line), and 10^{15} cm^{-2} (blue line) of 1.1 MeV protons.

Table 1. Average concentrations measured at widths *w* of the SCR before and after proton irradiation.

Sample #	i	$F(i)$ (cm^{-2})	$n_s(i)$ (cm^{-3})	$w(i)$ (μm)	$n_s(i+1)$ (cm^{-3})	$w(i+1)$ (μm)	$R_c(i)$ (cm^{-1})
S1	0	0	3.4×10^{15}	0.8	1.2×10^{15}	1.2	0
	1	10^{14}	0	1.2	10^{14}	1.8	35
	2	10^{15}	0	1.8			1.2
S2	0	0	5.2×10^{18}	0.022	3×10^{18}	0.028	0
	1	10^{15}	0	0.028	3×10^{18}	0.035	5200
	2	10^{16}	0				300
S3	0	0	8.7×10^{19}	0.0052	8.8×10^{19}	0.052	0
	1	10^{16}	8.8×10^{19}	0.0052			300

the light off and could not be quenched by the application of forward bias [18]. The concentrations were 2.3×10^{14} cm^{-3}, 6.9×10^{14} cm^{-3}, and 4.9×10^{14} cm^{-3}, respectively. These increased after irradiation with 10^{15} cm^{-2} 1.1 MeV protons to 6.6×10^{14} cm^{-3}, 2×10^{15} cm^{-3}, and 1.2×10^{15} cm^{-3} (figures 4(a) and (b)).

The results for the more heavily doped sample S2 are summarized in figures 5–7. Figure 5 shows the changes in room temperature *C–f* before and after irradiation. No low frequency step due to the 'slow' donors was observed and low-temperature AS were dominated by 0.15 eV and 0.25 eV donors, the shallower donors mostly contributing to the measured net donor density at 25 °C. The capacitance decreased after irradiation at 10^{15} cm^{-2}. Figure 6(a) displays the room temperature $1/C^2$–V plots obtained at 10 kHz frequency before and after irradiation with 10^{15} cm^{-2} and 10^{16} cm^{-2}. The slope at lower voltages probing the region closer to the surface is considerably steeper than deeper inside the sample, pointing to nonuniform distribution of respective centers. The net donor concentration profiles calculated from these plots are shown in figure 6(b). After irradiation with 10^{15} cm^{-2} dose, all shallow donors between 0.018 and 0.025 μm have been compensated, which implies the average concentration of shallow donors to be compensated as $\sim 5.5 \times 10^{18}$ cm^{-3} and an average carrier removal rate of 5.5×10^3 cm^{-1}. For the 10^{16} cm^{-2} fluence, all donors between 0.027 and 0.033 mm have been removed, indicating an average removal rate of ~ 300 cm^{-1}.

We measured the concentration of all deep centers throughout the entire bandgap by photocapacitance spectra measurements, which yield the spectral dependence of electrons within the SCR that can be excited from deep acceptors. The optical thresholds corresponding to the excitation of the deep acceptors were calculated, along with their densities [8, 25]. Figure 7 presents photocapacitance spectra measured with bias of 0 V at 10 kHz for the virgin sample and the sample irradiated with fluence of 10^{15} cm^{-2}. The *y*-axis, as in figures 4(a) and (b), is the value of photogenerated electrons concentration $N_{ph} = 2N_d \times \Delta C_{ph}/C_{dark}$. The net donor concentration in the dark, N_d, was taken from the carrier concentration plots in figure 6(b), with N_d corresponding to the 0 V bias at which the photocapacitance spectra were obtained. Centers with optical ionization thresholds of 2 eV, 2.8 eV and 3.1 eV are present, with concentrations of 2.8×10^{15} cm^{-3}, 2.8×10^{16} cm^{-3} and 10^{16} cm^{-3}, respectively (figure 6(b)).

For sample S3, a change in *C–f* characteristics could be detected only after irradiation with the fluence of 10^{16} cm^{-2},

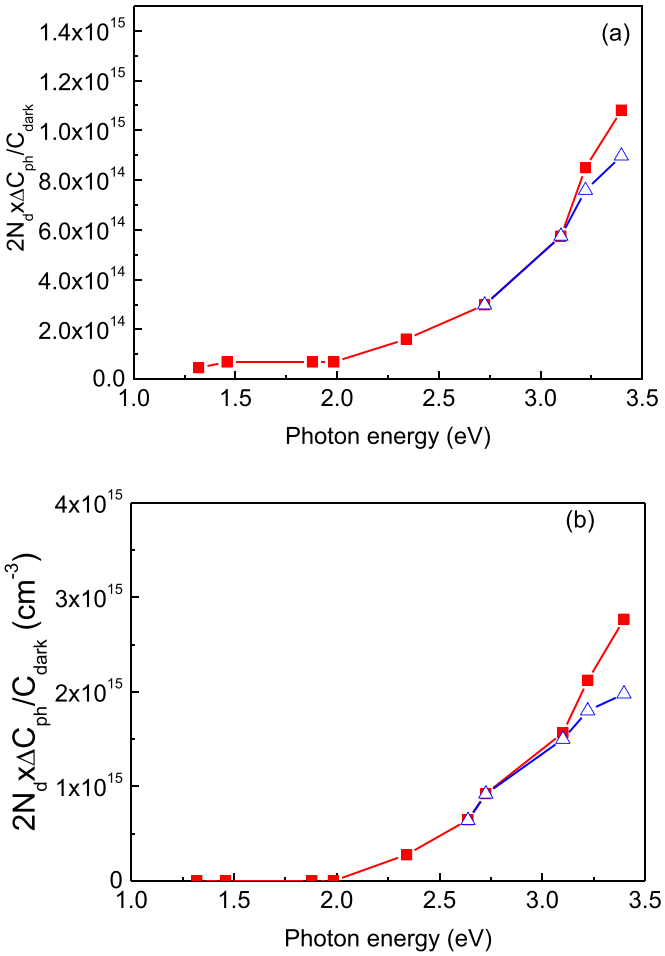

Figure 4. Photocapacitance spectra measured for the lightly doped sample S1 before irradiation (a) and after irradiation with 10^{15} cm^{-2} 1.1 MeV protons (b); solid red squares are the values obtained under irradiation, open blue triangles are the results obtained after switching off light and applying forward bias of +2 V for 10 s.

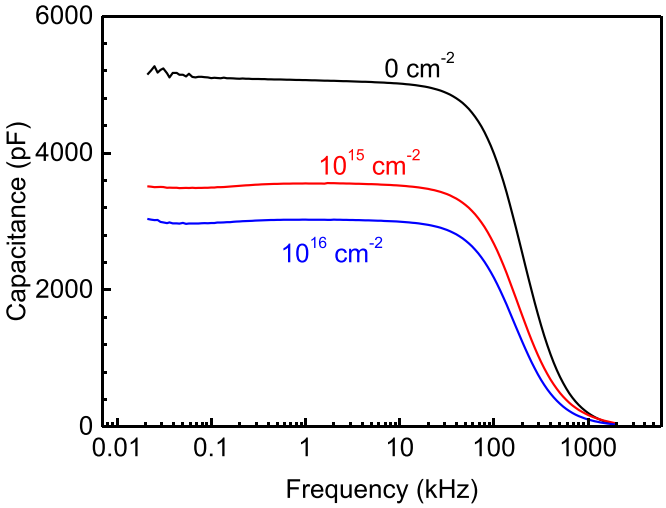

Figure 5. Room temperature *C–f* characteristics measured at 0 V for sample S2 before irradiation (black line), after irradiation with 10^{15} cm^{-2} (red line), and after irradiation with 10^{16} cm^{-2} 1.1 MeV protons (blue line).

as shown in figure 8(a). Figure 8(b) shows the resultant changes induced in $1/C^2$ versus V characteristics. The initial net donor concentration of 8.7×10^{19} cm^{-3} decreased to 8.4×10^{19} cm^{-3} after irradiation with 10^{16} cm^{-2}. The effective carrier removal rate was 300 cm^{-1} similar to that of sample S2. The concentration profiles are shown in figure S2 of the supplementary material.

I–V's for both types of lightly doped samples showed the characteristics were not affected by irradiation to the fluence of 10^{16} cm^{-2} (see figures S3 and S4 of supplementary material).

DLTS spectra measurements were not informative. In all cases, the signal was dominated by an electron trap at E_c-1 eV and electron capture cross section $\sim 10^{-13}$ cm^2. The concentrations of these centers did not change after irradiation (figures S4–S6 of the supplementary material show respective spectra for samples S1–S3). Figure 9 summarizes the defect levels observed in our experiments and their possible assignations.

The electron removal rates by 1.1 MeV protons for donor concentrations of 10^{16} or 3.5×10^{18} cm^{-3} increase with starting concentration from $\sim$35 cm^{-1}–5.5×10^3 cm^{-1} and decrease with fluence to respectively $\sim$1.3 cm^{-1} and 300 cm^{-1}. For the heavily doped sample, changes could be detected only after fluence of 10^{16} cm^{-2}. Figure 10 summarizes these findings.

The range of donor concentrations studied covers all important possible applications of α-Ga_2O_3 devices, from photodetectors to FETs. Then it is interesting to compare with existing data for the beta polymorph, and to understand possible mechanisms of electron removal by protons. For samples with starting concentration of 10^{16} cm^{-3} and protons with energy 0.6–1.7 MeV, there have been reported initial removal rates of $\sim 2 \times 10^3$ cm^{-1}, about half an order of magnitude lower than the carrier removal rate estimated from modeling if one assumes that no dynamic annealing of primary radiation defects occurs [16, 39]. This indicates a higher radiation tolerance of lightly doped α-Ga_2O_3 films compared to β-Ga_2O_3 films. This could be due to a higher density of extended defects in α-Ga_2O_3 films. The total concentration of deep acceptors introduced by protons in lightly doped α-Ga_2O_3 film S1, as deduced from photocapacitance spectra measurements after irradiation with 10^{15} cm^{-2} protons, is on the same order as would be required to explain the observed carrier removal rate. Recent theoretical modeling [40] suggests that the centers responsible could be due to the triply charged Ga vacancies $V_{Ga}{}^{3-}$.

For the more heavily doped sample S2, the starting carrier removal rate is much higher, $\sim 5 \times 10^3$ cm^{-1}, and different from modeling assuming compensation by the primary radiation defects, V_{Ga} [16]. The types of deep acceptors visible in photocapacitance spectra is the same as for the lightly doped sample S1, but their total number after irradiation with 10^{16} cm^{-2}, about 4×10^{16} cm^{-3} falls far short of the carrier removal rate at the 10^{16} cm^{-2} fluence ($\sim$300 cm^{-1}). This suggests that, rather than direct compensation of shallow donors

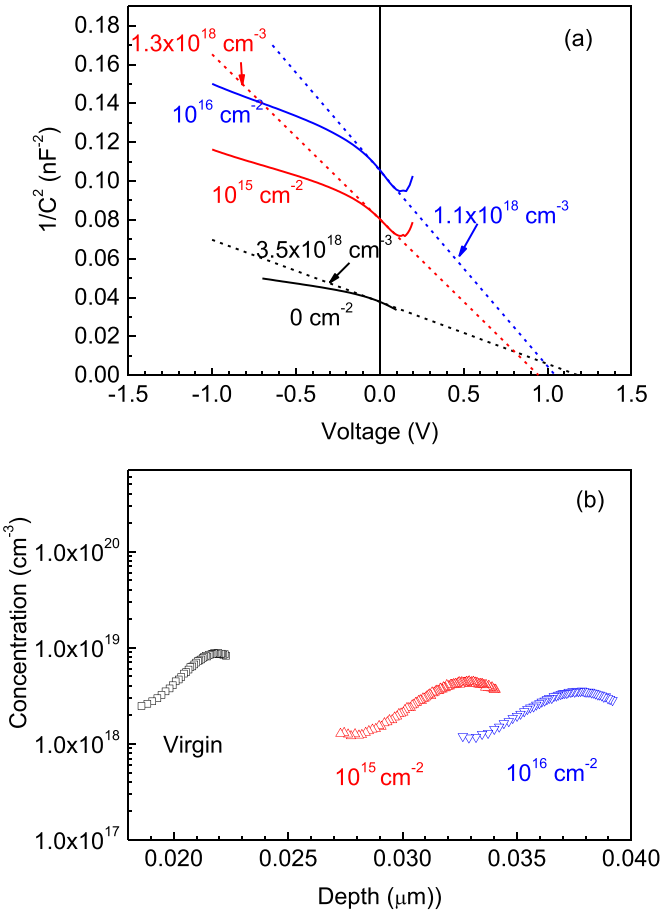

Figure 6. (a)$1/C^2$ versus V plots obtained at 10 kHz for sample S2 before (virgin sample, black line), after irradiation with 10^{15} cm^{-2} (red line), and 10^{16} cm^{-2} (blue line) fluences of 1.1 MeV protons; labels near the dashed lines show the net donor concentrations calculated from low-voltage slopes; (b) concentration profiles calculated from the data in (a).

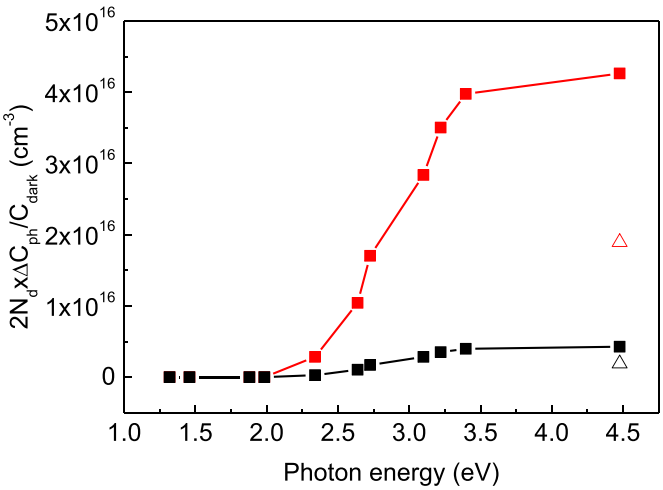

Figure 7. Photocapacitance spectra of sample 2 measured at 0 V, solid black squares are for the virgin sample, solid red squares for the sample irradiated with 10^{16} cm^{-2} protons, open triangles are for measurements after switching off light and application of +2 V for 10 s.

with V_{Ga}-like acceptors that would be detectable in photocapacitance spectra, there may be complexing of V_{Ga} with shallow donors, removing their electrical effect. For the two more lightly doped samples, the changes in the carrier concentration profiles occur faster nearer to the surface, suggesting the radiation defects migrate towards the surface where

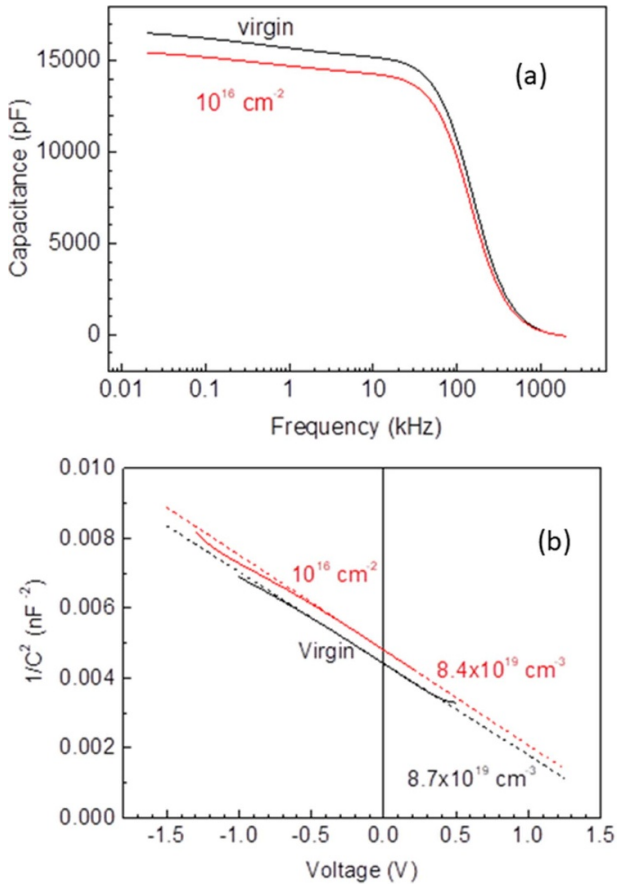

Figure 8. (a) Room temperature *C–f* characteristics measured at 0 V for sample S3 before and after irradiation with 10^{16} cm^{-2} protons. (b) $1/C^2$ versus voltage plots for sample S3 before and after irradiation with 10^{16} cm^{-2} protons. The dashed lines indicate fits to the data to extract effective carrier density.

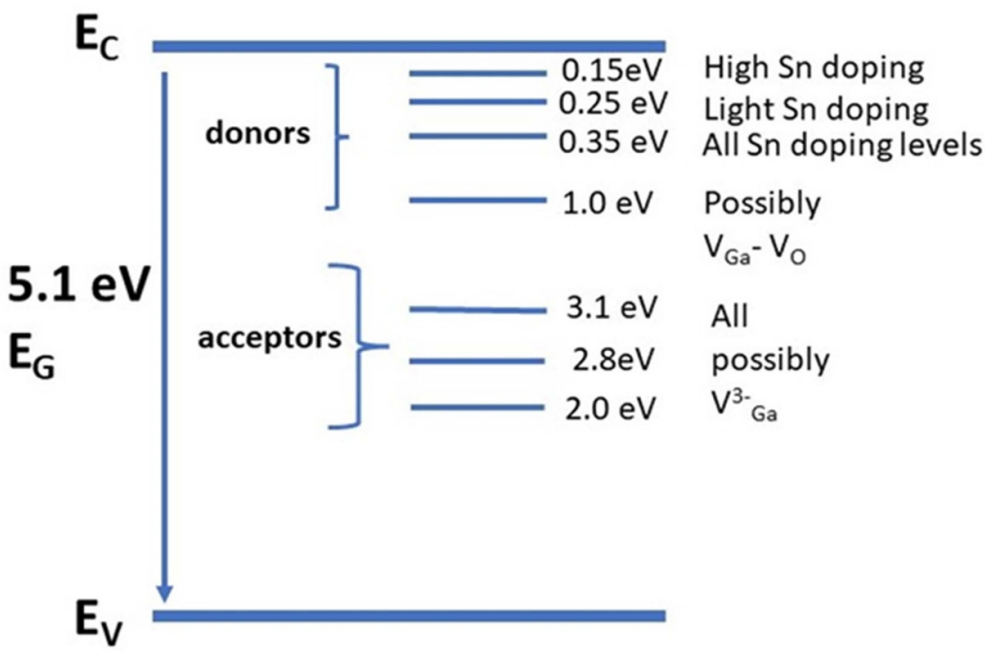

Figure 9. Schematic of energy levels of defects with in the α-Ga_2O_3 bandgap.

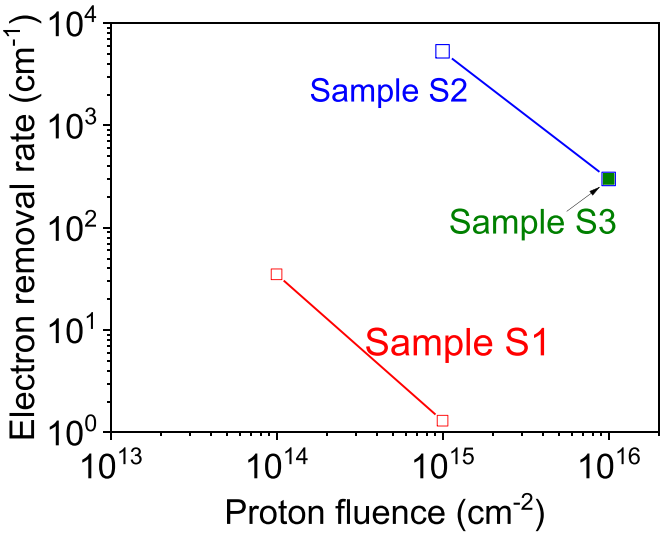

Figure 10. Carrier removal rates as a function of proton fluence for the three studied samples.

they either compensate the existing shallow donors or passivate them by forming complexes. In the latter case, Ga vacancies are strongly suspected and the change of the complexing efficiency with donor concentration could be the result of competition between forming the complexes with donors and dynamic recombination.

We observe the carrier removal rate increasing with starting donor density and decreasing with increasing fluence (figure 10). For the heavily doped sample S2, the removal rate at lower fluence of 10^{15} cm^{-2} is not too different from the modeling result, while for the higher proton fluence, the experimental removal rate is far less than predicted and cannot be attributed to compensation by deep acceptor states visible in photocapacitance spectra. It could be assumed that, for high starting donor concentrations, the dominant process becomes formation of neutral complexes of shallow donors and deep native defects acceptors, likely V_{Ga}, while, with higher fluence, the dynamic recombination of primary defects becomes more pronounced, thus decreasing the carrier removal rate. This assumption could be checked by doing measurements with high and low proton fluxes when accumulating the same final proton fluence.

In lightly doped sample S1, the density of shallow donors is too small to effectively bind the Ga vacancies and prevent them from being lost in dynamic recombination processes or being trapped by dislocations, while, whatever defects survive, form deep compensating acceptors visible in photocapacitance spectra and accounting for the observed removal rate.

The deep traps near E_c-1 eV visible in DLTS are not far in energy from deep donors due to V_{Ga}–V_O divacancies or O interstitials [40]. Their role in compensation is negligible because they are deep donors. One has to assume from DLTS spectra measurements results their introduction rate is small. Under some conditions, one could even expect the density of these deep donors could decrease with irradiation due to interaction with primary native radiation defects.

4. Conclusions

We measured carrier removal rates by 1.1 MeV proton irradiation of α-Ga_2O_3 having initial net donor concentrations of 5×10^{15} cm^{-3}, 4×10^{18} cm^{-3} and 8.4×10^{19} cm^{-3}. For the lightly doped samples, the electron removal rate with 10^{14} cm^{-2} protons was 35 cm^{-1} and decreased to 1.3 cm^{-1} for 10^{15} cm^{-2}. Deep acceptors were introduced in the lower half of the bandgap with optical ionization thresholds of 2 eV, 2.8 eV and 3.1 eV and introduction rates compatible with the observed experimental electron removal rate. The removal rates in lightly doped α-Ga_2O_3 are significantly lower than for similarly doped β-Ga_2O_3. This could be an advantage of lightly doped α-Ga_2O_3 over β-Ga_2O_3 in applications requiring high radiation tolerance if the starting performance could be made comparable.

In more heavily doped samples, the initial electron removal rate was 5×10^3 cm^{-2}, but decreased to 300 cm^{-1} for fluences of 10^{16} cm^{-2}. The deep acceptors introduced were the same as for lightly doped samples, but their introduction rates were lower than the electron removal rates, suggesting carrier removal could be due to complexing of primary radiation-produced native acceptors with shallow donors. For the most heavily doped samples, electron removal could be detected only after irradiation with the fluence of 10^{16} cm^{-2} and the removal rate was close to that for moderately doped samples, $\sim$300 cm^{-1}.

Data availability statement

All data that support the findings of this study are included within the article (and any supplementary files).

Acknowledgments

The work at NUST MISiS was supported in part by a grant from the Ministry of Science and Higher Education of Russian

Federation (Agreement # 075-15-2022-1113). The work at UF was performed under the Interaction of Ionizing Radiation with Matter University Research Alliance (IIRM-URA), sponsored by Department of Defense, Defense Threat Reduction Agency under Award HDTRA1-20-2-0002. The work at UF was also supported by NSF DMR 1856662.

ORCID iDs

Yu S Pavlov https://orcid.org/0000-0003-0540-8286
R Sh Isaev https://orcid.org/0000-0003-2952-2825
S J Pearton https://orcid.org/0000-0001-6498-1256

References

[1] Higashiwaki M and Fujita S (eds) 2020 *Gallium Oxide: Materials Properties, Crystal Growth, and Devices* (*Springer Series in Materials Science*) (Berlin: Springer)
[2] Pearton S J, Ren F, Tadjer M and Kim J 2018 Perspective: Ga_2O_3 for ultra-high power rectifiers and MOSFETS *J. Appl. Phys.* **124** 220901
[3] Xu J, Zheng W and Huang F 2019 Gallium oxide solar-blind ultraviolet photodetectors: a review *J. Mater. Chem.* C **7** 8753–70
[4] Zhang J *et al* 2022 Ultra-wide bandgap semiconductor Ga_2O_3 power diodes *Nat. Commun.* **13** 3900
[5] Oshima Y and Ahmadi E 2022 Progress and challenges in the development of ultra-wide bandgap semiconductor α-Ga_2O_3 toward realizing power device applications *Appl. Phys. Lett.* **121** 260501
[6] Biswas M and Nishinaka H 2022 Thermodynamically metastable α-, ε- (or κ-), and γ-Ga_2O_3: from material growth to device applications *APL Mater.* **10** 060701
[7] Anhar Uddin Bhuiyan A F M, Feng Z, Huang H-L, Meng L, Hwang J and Zhao H 2021 Metalorganic chemical vapor deposition of α-Ga_2O_3 and α-$(Al_xGa_{1-x})_2O_3$ thin films on m-plane sapphire substrates *APL Mater.* **9** 101109
[8] Shinohe T 2022 *Proc. Int. Power Electronics Conf. (IPEC-Himeji 2022-ECCE Asia)* (Himeji: IEEE) pp 627–31 (available at: www.proceedings.com/64438.html)
[9] McCandless J P *et al* 2021 Thermal stability of epitaxial α-Ga_2O_3 and $(Al,Ga)_2O_3$ layers on m-plane sapphire *Appl. Phys. Lett.* **119** 062102
[10] Son H, Choi Y-J, Park J-H, Ryu B and Jeon D-W 2020 Correlation of pulsed gas flow on Si-doped α-Ga_2O_3 epilayer grown by halide vapor phase epitaxy *ECS J. Solid State Sci. Technol.* **9** 055005
[11] Kaneko K, Masuda Y, Kan S-I, Takahashi I, Kato Y, Shinohe T and Fujita S 2021 Ultra-wide bandgap corundum-structured p-type α-$(Ir,Ga)_2O_3$ alloys for α-Ga_2O_3 electronics *Appl. Phys. Lett.* **118** 102104
[12] Hao J G, Gong H H, Chen X H, Xu Y, Ren -F-F, Gu S L, Zhang R, Zheng Y D and Ye J D 2021 *In situ* heteroepitaxial construction and transport properties of lattice-matched α-Ir_2O_3/α-Ga_2O_3 p-n heterojunction *Appl. Phys. Lett.* **118** 261601
[13] Venzie A, Portoff A, Michael Stavola W, Fowler B, Kim J, Jeon D-W, Park J-H and Pearton S J 2022 H trapping at the metastable cation vacancy in α-Ga_2O_3 and α-Al_2O_3 *Appl. Phys. Lett.* **120** 192101
[14] Ahmadi E and Oshima Y 2019 Materials issues and devices of α- and β-Ga_2O_3 *J. Appl. Phys.* **126** 160901
[15] Kaneko K, Fujita S and Hitora T 2018 A power device material of corundum-structured α-Ga_2O_3 fabricated by MIST EPITAXY technique *Jpn. J. Appl. Phys.* **57** 02CB18
[16] Polyakov A Y, Nikolaev V I, Yakimov E B, Ren F, Pearton S J and Kim J 2022 Deep level defect states in β-, α-, and ε-Ga_2O_3 crystals and films: impact on device performance *J. Vac. Sci. Technol.* A **40** 020804
[17] Artús S L, Cuscó R, Goldhahn R and Feneberg M 2017 Band gap of corundumlike α-Ga_2O_3 determined by absorption and ellipsometry *Phys. Rev. Mater.* **1** 024604
[18] Polyakov A Y *et al* 2020 Electrical properties and deep traps in α-Ga_2O_3:Sn films grown on sapphire by halide vapor phase epitaxy *ECS J. Solid State Sci. Technol.* **9** 045003
[19] Polyakov A Y *et al* 2019 Deep trap spectra of Sn-doped α-Ga_2O_3 grown by halide vapor phase epitaxy on sapphire *APL Mater.* **7** 051103
[20] Bae J, Park J-H, Jeon D-W and Kim J 2021 Self-powered solar-blind α-Ga_2O_3 thin-film UV-C photodiode grown by halide vapor-phase epitaxy *APL Mater.* **9** 101108
[21] Fujita S, Oda M, Kaneko K and Hitora T 2016 Evolution of corundum-structured III-oxide semiconductors: growth, properties, and devices *Jpn. J. Appl. Phys.* **55** 1202A3
[22] Oshima Y, Kawara K, Shinohe T, Hitora T, Kasu M and Fujita S 2019 Epitaxial lateral overgrowth of α-Ga_2O_3 by halide vapor phase epitaxy *APL Mater.* **7** 022503
[23] Jinno R, Uchida T, Kaneko K and Fujita S 2016 Reduction in edge dislocation density in corundum-structured α-Ga_2O_3 layers on sapphire substrates with quasi-graded α-$(Al,Ga)_2O_3$ buffer layers *Appl. Phys. Express* **9** 071101
[24] Polyakov A *et al* 2022 Electrical properties of α-Ga_2O_3 films grown by halide vapor phase epitaxy on sapphire with α-Cr_2O_3 buffers *J. Appl. Phys.* **131** 215701
[25] Polyakov A *et al* 2022 Effects of sapphire substrate orientation on Sn-doped α-Ga_2O_3 grown by halide vapor phase epitaxy using α-Cr_2O_3 buffers *J. Appl. Phys.* **55** 495102
[26] Kim J, Pearton S J, Fares C, Yang J, Fan R, Kim S and Polyakov A Y 2018 Radiation damage effects in Ga_2O_3 materials and devices *J. Mater. Chem.* C **7** 10
[27] Xia X *et al* 2022 Radiation damage in the ultra-wide bandgap semiconductor Ga_2O_3 *ECS J. Solid State Sci. Technol.* **11** 095001
[28] McGlone J F, Ghadi H, Cornuelle E, Armstrong A, Burns G, Zixuan Feng A F M, Bhuiyan A U, Zhao H, Arehart A R and Ringel S A 2023 Proton radiation effects on electronic defect states in MOCVD-grown (010) β-Ga_2O_3 *J. Appl. Phys.* **133** 045702
[29] Titov A, Karabeshkin K, Struchkov A, Nikolaev V, Azarov A, Gogova D and Karaseov P 2022 Comparative study of radiation tolerance of GaN and Ga_2O_3 polymorphs *Vacuum* **200** 111005
[30] Polyakov A Y *et al* 2022 Point defect creation by proton and carbon irradiation of α-Ga_2O_3 *J. Appl. Phys.* **132** 035701
[31] Li J V and Ferrari G (eds) 2018 *Capacitance Spectroscopy of Semiconductors* (Singapore: Pan Stanford Publishing Pte Ltd) p 437
[32] Polyakov A Y, Smirnov N B, Shchemerov I V, Pearton S J, Ren F, Chernykh A V, Lagov P B and Kulevoy T V 2018 Hole traps and persistent photocapacitance in proton irradiated β-Ga_2O_3 films doped with Si *APL Mater.* **6** 096102
[33] Polyakov A Y, Smirnov N B, Shchemerov I V, Yakimov E B, Pearton S J, Fan Ren A V, Gogova C D, Kochkova A I, Properties E and Trap D 2019 Luminescence spectra in semi-insulating, Czochralski β-Ga_2O_3 (Mg) *ECS J. Solid State Sci. Technol.* **8** Q3019–23
[34] Polyakov A Y *et al* 2018 Defects responsible for charge carrier removal and correlation with deep level introduction in irradiated β-Ga_2O_3 *Appl. Phys. Lett.* **113** 092102

[35] Polyakov A Y *et al* 2021 Crystal orientation dependence of deep level spectra in proton irradiated bulk β-Ga_2O_3 *J. Appl. Phys.* **130** 035701
[36] Polyakov A Y *et al* 2021 1 GeV proton damage in β-Ga_2O_3 *J. Appl. Phys.* **130** 185701
[37] Zhang Z, Farzana E, Arehart A R and Ringel S A 2016 Deep level defects throughout the bandgap of (010) β-Ga_2O_3 detected by optically and thermally stimulated defect spectroscopy *Appl. Phys. Lett.* **108** 052105
[38] Boschini M J, Rancoita P G and Tacconi M 2014 SR-NIEL-7 calculator: screened relativistic (SR) treatment for calculating the displacement damage and nuclear stopping powers for electrons, protons, light- and heavy- ions in materials (version 9.0) (Milano-Bicocca) (available at: www.sr-niel.org/) (Accessed February 2023)
[39] Ingebrigtsen M E, Kuznetsov A Y, Svensson B G, Alfieri G, Mihaila A, Badstubner U, Perron A, Vines L and Varley J B 2019 Impact of proton irradiation on conductivity and deep level defects in β-Ga_2O_3 *APL Mater.* **7** 022510
[40] Kobayashi T, Gake T, Kumagai Y, Oba F and Matsushita Y-I 2019 Energetics and electronic structure of native point defects in α-Ga_2O_3 *Appl. Phys. Express* **12** 091001